CMS Physics Analysis Summary

Contact: cms-pag-conveners-exotica@cern.ch 2013/06/27

Search for a W′ or ρ_{TC} decaying into WZ in pp collisions at $\sqrt{s} = 8$ TeV

The CMS Collaboration

Abstract

A search is performed in pp collisions at $\sqrt{s} = 8$ TeV for exotic particles decaying via WZ to final states with electrons and muons. The data sample corresponds to an integrated luminosity of 19.6 fb^{-1}. No significant excess is observed in the data above the expected standard model background. Upper bounds at 95% confidence level are set on the production cross section of the W' boson described by the sequential standard model, and on the $W'WZ$ coupling. W' bosons with masses between 170 and 1450 GeV are excluded. Limits are also set in the context of low-scale technicolor models, under a range of assumptions concerning the model parameters.

1 Introduction

Many extensions of the standard model (SM) predict new, heavy $W^{'}$ bosons that decay into a pair of W and Z bosons [1–6]. Searches in this channel have been performed at the Tevatron [7, 8] and at the LHC [9–11]. The search conducted by the Compact Muon Solenoid (CMS) experiment at $\sqrt{s} = 7$ TeV [10] set a limit of 1143 GeV for $W^{'}$ bosons decaying via a WZ pair with $W \to \ell\nu$ and $Z \to \ell\ell$ in the final state, where $\ell = e, \mu$. Limits were also set in the context of low-scale technicolor (LSTC) models [12, 13], under a range of assumptions concerning the model parameters.

This note describes an update of the analysis in Ref. [10] using data collected by the CMS experiment in 2012 at $\sqrt{s} = 8$ TeV corresponding to a total integrated luminosity of 19.6 fb^{-1}. As before, we analyze events in the tri-lepton channel and interpret the results within the context of the sequential standard model (SSM) and LSTC. The analysis benefits from the increase in center-of-mass energy and also from improvements in lepton identification and isolation, particularly at high transverse momentum (p_T). The isolation requirement used in the $\sqrt{s} = 7$ TeV analysis adversely impacted efficiency at high $W^{'}$ mass because the leptons from the boosted Z boson became more collimated. This drop in efficiency is recovered in the $\sqrt{s} = 8$ TeV analysis described below. Additional improvements related to a better optimization of selection criteria are also incorporated.

2 CMS Detector

The central feature of the CMS apparatus is a superconducting solenoid of 6 m internal diameter, providing a magnetic field of 3.8 T. Within the superconducting solenoid volume are a silicon pixel and strip tracker, a lead tungstate crystal electromagnetic calorimeter (ECAL), and a brass/scintillator hadron calorimeter. Muons are measured in gas-ionization detectors embedded in the steel return yoke outside the solenoid. Extensive forward calorimetry complements the coverage provided by the barrel and endcap detectors.

CMS uses a right-handed coordinate system, with the origin at the nominal interaction point, the x axis pointing to the center of the LHC, the y axis pointing up (perpendicular to the LHC plane), and the z axis along the anticlockwise-beam direction. The polar angle θ is measured from the positive z axis and the azimuthal angle ϕ is measured in the x-y plane. The pseudorapidity (η) is given by $\eta \equiv -\ln(\tan(\theta/2))$.

The ECAL energy resolution for electrons with $E_T \approx 45$ GeV from $Z \to ee$ decays is better than 2% in the central region of the ECAL barrel ($|\eta| < 0.8$), and is between 2% and 5% elsewhere. For low-bremsstrahlung electrons, where 94% or more of their energy is contained within a 3×3 array of crystals, the energy resolution improves to 1.5% for $|\eta| < 0.8$.

Muons are measured in the pseudorapidity range $|\eta| < 2.4$, with detection planes made using three technologies: drift tubes, cathode strip chambers, and resistive plate chambers. Matching muons to tracks measured in the silicon tracker results in a transverse momentum resolution between 1 and 5%, for p_T values up to 1 TeV.

A more detailed description of the CMS detector can be found elsewhere [14].

3 Monte Carlo Samples

The $W^{'}$ signal and SM background samples used in this analysis were produced using full GEANT4 [15] simulation of the CMS detector. Pileup reweighting was applied to all the Monte

Carlo samples in order to simulate the additional proton-proton interactions in each bunch crossing. Other details pertaining to the simulation are described below.

3.1 Signal Simulation

The generator PYTHIA 6.42 [16] and the CTEQ6L1 [17] parton distribution functions (PDF) were used for producing the $W^{'}$ and ρ_{TC} samples. For the detailed simulation of the $W^{'}$ samples, PYTHIA was used for parton showering and hadronization and the tune Z2* [18] was used for the underlying event simulation. Only the leptonic decays of the vector bosons ($W \to \ell\nu$ and $Z \to \ell^{+}\ell^{-}$) with $\ell = e, \mu, \tau$ are included with the contribution of the leptonic decays of τ's from the W or Z boson being considered as a background. The full list of $W^{'}$ signal samples, including their cross sections, are presented in Table 1. The cross sections listed are scaled to next-to-next-to-leading order (NNLO) values with the *k*-factors taken from Ref. [19].

For the LSTC study we assume that the techni-hadrons, ρ_{TC} and a_{TC}, decay to WZ boson pairs. Since these two states are expected to be nearly mass-degenerate [13], they would appear as a single feature in the WZ invariant mass spectrum, and we hereafter refer to them collectively as ρ_{TC}. We consider the same relationship between techni-hadrons ρ_{TC} and π_{TC} as used in the Les Houches study [20] and Ref. [10], $M(\pi_{TC}) = \frac{3}{4}M(\rho_{TC}) - 25$ GeV, and also investigate the dependence of the results on the relative values of the ρ_{TC} and π_{TC} masses. Since we do not expect a difference in the kinematics between the $W^{'}$ and LSTC signals, we use the $W^{'}$ samples as the default for the analysis with the cross sections for LSTC as given by PYTHIA. This strategy is identical to Ref. [10].

Table 1: An overview of the $W^{'} \to WZ \to \ell\nu\ell\ell$ signal samples considered in this analysis, giving the $W^{'}$ mass along with the associated NNLO cross section in the SSM. The cross sections include the branching ratios for the bosonic decays into electrons and muons. The *k*-factors used are also given along with the full width at half maximum (FWHM) for each $W^{'}$ mass for the four channels combined. The generator-level widths are denoted as "Gen." while the widths dominated by the detector resolution are denoted as "Reco.". The "Reco." widths are dominated by the channels with two or more muons.

$W^{'}$ Mass (GeV)	σ_{NNLO} (pb)	k_{NNLO}	Gen. FWHM (GeV)	Reco. FWHM (GeV)
200	9.6146e-01	1.347	6	36
300	4.5654e-01	1.347	10	52
400	1.5321e-01	1.355	13	66
500	6.1365e-02	1.363	17	71
600	2.8177e-02	1.357	20	80
700	1.4477e-02	1.351	24	85
800	7.9261e-03	1.349	29	90
900	4.6480e-03	1.347	31	94
1000	2.7964e-03	1.339	33	100
1100	1.7380e-03	1.331	40	108
1200	1.1233e-03	1.324	42	126
1300	7.4864e-04	1.317	45	147
1400	5.0385e-04	1.305	49	159
1500	3.3474e-04	1.293	54	168
1600	2.2769e-04	1.275	56	173
1700	1.5844e-04	1.257	61	179
1800	1.1086e-04	1.244	63	186
1900	7.8611e-05	1.230	66	197
2000	5.5736e-05	1.214	76	208

3.2 Background Simulation

The background processes were generated using the MADGRAPH 5.1 [21] and POWHEG 1.1 [22] generators interfaced to PYTHIA 6.42 for parton showering, hadronization and simulation of the underlying event. The simulated backgrounds include irreducible processes which produce the same final state as the signal as well as reducible processes which produce different physics, but lead to similar signals in the detector. The physics backgrounds are dominated by the SM WZ process which was generated using the MADGRAPH 5.1 generator. Also included was the ZZ process (generated using POWHEG 1.1) where one of the leptons is either outside the detector acceptance or mis-reconstructed. The instrumental backgrounds are due to mis-identified lepton candidates from jets and photons. These background processes were produced using MADGRAPH and include Z+jets, $t\bar{t}$, $Z\gamma$, WW+jets, and W+jets. The background from QCD multi-jet events and from $W/\gamma^{\star}$ was also studied in the simulation and found to be negligible. Next-to-leading order (NLO) cross sections are used with the exception of the W+jets process for which the NNLO cross section is used.

4 Object Reconstruction and Event Selection

The WZ $\rightarrow 3\ell\nu$ decay is characterized by a pair of same-flavor, opposite-charge, high-p_{T} isolated leptons with an invariant mass corresponding to a Z boson, a third, high-p_{T} isolated lepton, and a significant amount of missing transverse energy ($E_{\mathrm{T}}^{\mathrm{miss}}$) associated with an escaping neutrino. The analysis, therefore, relies on the reconstruction of three types of objects: electrons, muons and $E_{\mathrm{T}}^{\mathrm{miss}}$. The events are reconstructed using a full particle-flow approach [23, 24] and the details of the selection are provided below.

Candidate events are required to have at least three reconstructed leptons within the detector acceptance of $|\eta| < 2.5(2.4)$ for electrons (muons). The events are triggered using a double-electron or double-muon trigger for final states with the Z decaying into electrons or muons, respectively. The trigger requirements are different from the 7 TeV analysis [10] in order to improve sensitivity for leptons from boosted Z bosons. The double-electron trigger requires two clusters in the electromagnetic calorimeter with transverse energy $E_T > 33$ GeV. The spread of the energy deposits comprising the cluster in η is required to be loosely compatible with that of an electron. The trigger also requires that the sum of the energy of the hadron calorimeter cells in a cone of $\Delta R < 0.14$ (where $\Delta R = \sqrt{(\Delta\phi)^2 + (\Delta\eta)^2}$) centered on the cluster be no more than 15% (10%) of the clusters energy in the barrel (endcap) region of the electromagnetic calorimeter. Finally, the clusters are required to be loosely matched in η and ϕ to an online track with hits in the pixel detector.

The double-muon trigger requires a "global" muon with $p_{\mathrm{T}} > 22$ GeV and a "tracker" muon with $p_{\mathrm{T}} > 8$ GeV. The global muon is reconstructed using an "outside-in" approach whereby each standalone muon track is matched to a tracker track by comparing parameters of the two tracks. The tracker muon is reconstructed using an "inside-out" approach in which all tracker tracks with $p_{\mathrm{T}} > 0.5$ GeV and total momentum $p > 2.5$ GeV are considered as possible muon candidates and are extrapolated to the muon system taking into account the magnetic field, the average expected energy losses, and multiple Coulomb scattering in the detector material. If at least one muon segment matches the extrapolated track, the corresponding tracker track qualifies as a tracker muon. [25].

Trigger efficiencies are measured using the tag-and-probe technique [26] and are used for appropriately weighting the simulated events. Data-to-simulation scale factors are also applied to the simulated samples to account for differences in the muon(electron) trigger efficiency. In

the electron channel, we apply a scale factor of 99.5% to account for the trigger efficiency and also a parametrization based on the turn-on curve observed in data. Muon trigger efficiencies on the plateau are typically above 80% in data and the scale factors agree with unity to within 4%.

Leptons from the W and Z decays are also required to pass a series of identification and isolation criteria to reduce background from jets being misidentified as leptons. These criteria are described below.

4.1 Electron Selection

Electron candidates are reconstructed from a collection of electromagnetic clusters with matched pixel tracks. The momentum of the electron track is fitted using a Gaussian Sum Filter algorithm [27] along its trajectory with the algorithm taking into account the possible emission of Bremsstrahlung photons in the silicon tracker. The following requirements are imposed:

- $p_{\mathrm{T}}(\mathrm{e}) > 35$ GeV for the electrons from the Z decay and $p_{\mathrm{T}}(\mathrm{e}) > 20$ GeV for the electron from the W decay.
- $|\eta(\mathrm{e})| < 2.5$; we also exclude the barrel and endcap transition region ($1.4442 < |\eta| < 1.566$).
- "Loose" identification requirement for the electrons from the Z decays and "Medium" requirement for the electrons from the W decays.
- Particle-flow based relative isolation, I_{rel}, is required to be less than 0.15, where I_{rel} is defined as the sum of the transverse momenta of all neutral and charged reconstructed particle candidates inside a cone around the electron in $\eta - \phi$ space of $\Delta R < 0.3$, divided by the p_{T} of the electron. The sum is also corrected for pileup.

Finally, electron/muon ambiguities arise due to photons from internal Bremsstrahlung in W and Z decays which can generate a fake electron aligned with the muon. In order to remove such ambiguities, electrons are rejected if they are within a cone of $\Delta R < 0.01$ around a muon.

Data-to-simulation scale factors binned in electron p_T and η are applied as corrections to the simulated samples.

4.2 Muon Selection

The muon selection is optimized for the selection of high$-p_{\mathrm{T}}$ muons. The following requirements are imposed:

- Leading (sub-leading) muon $p_{\mathrm{T}} > 25(10)$ GeV for the muons from the Z decay and $p_{\mathrm{T}} > 20$ GeV for the muon from the W decay.
- $|\eta| < 2.4$.
- Muon is required to be classified as a global (tracker + muon system) muon.
- Number of muon chamber hits included in the global muon track fit > 0.
- Number of muon stations with matched segments > 1.
- Transverse impact parameter of the tracker track with respect to the primary vertex $d_{xy} < 2$ mm.
- Longitudinal distance of the tracker track with respect to the primary vertex $d_z < 5$ mm.
- Number of pixel hits > 0.

- Number of tracker layers with hits > 5.
- Require $\Delta p_T / p_T < 0.3$ for the track used for the momentum determination.
- Particle-flow based relative isolation, I_{rel}, for a cone of size $\Delta R = 0.4$ is required to be less than 0.12. The isolation sum is corrected for pileup.
- The above criteria are modified slightly for muons coming from the Z boson decay. One of the leptons is allowed to be a tracker muon instead of a global muon and the requirement on the number of muon chamber hits is removed. Additionally, the isolation variable for each lepton is modified to remove the contribution of the other lepton. These modifications improve the signal efficiency for high mass W$'$ bosons.

Data-to-simulation scale factors binned in muon p_{T} and η are applied as corrections to the simulated samples.

4.3 Missing Transverse Energy

Neutrinos from the leptonic W boson decay do not interact with the detector and result in a significant missing transverse energy, $E_{\text{T}}^{\text{miss}}$, in the event. The $E_{\text{T}}^{\text{miss}}$ in these analyses is calculated with the particle-flow method [23]. The algorithm allows for precise corrections to particle energies and also provides a significant degree of redundancy, which renders the $E_{\text{T}}^{\text{miss}}$ measurement less sensitive to calorimetry miscalibration. The $E_{\text{T}}^{\text{miss}}$ is computed as the magnitude of the negative vector sum of transverse energies of all particle-flow objects and the following requirement is imposed:

- $E_{\text{T}}^{\text{miss}} > 30$ GeV.

4.4 WZ Selection

Z candidates are built from two opposite-sign, same-flavor leptons. The leading and second leading lepton are required to have $p_{\text{T}} > 35$ GeV for the Z $\rightarrow ee$ channel and $p_{\text{T}} > 25$ and 10 GeV for the Z $\rightarrow \mu\mu$ case. The choice of these selection criteria ensures that the offline threshold is in the plateau region of the trigger turn-on with an efficiency larger than 98%. The Z candidate invariant mass should lie between 71 and 111 GeV. In the case of more than one matching pair, the Z candidate with the mass closest to the nominal Z mass is selected. Events with two non-overlapping Z candidates are rejected in order to suppress the ZZ background.

A lepton from a W boson leptonic decay is then selected out of the remaining leptons requiring $p_{\text{T}} > 20$ GeV. In case several candidates are found, the one with the highest p_{T} is selected. The missing transverse energy in the event is then required to be larger than 30 GeV to select W boson decays. This requirement discriminates against high-p_{T} jets mis-identified as leptons or photon conversions from Z+jets or Zγ events, respectively.

In order to supress events where final-state radiation produces additional leptons that are identified as the W lepton, we apply two additional requirements on the event after the W lepton selection. First, events where $m_{3\ell} < 120$ GeV are rejected to remove events where the tri-lepton invariant mass is close to the Z mass. Second, events where the ΔR between either Z lepton and the W lepton is less than 0.3 are rejected. This removes cases where the W lepton comes from a converted photon and is unlikely to occur in the boosted topology of a high mass W$'$.

After both a W and Z candidate are chosen, the two are combined into a WZ candidate. The invariant mass of this candidate cannot be determined uniquely since the longitudinal momentum of the neutrino is unknown. We estimate the invariant mass of the WZ candidate by making two assumptions. By assuming the mass of the W, we reduce the longitudinal momentum

of the neutrino p_z^ν to a quadratic equation. We find that the less energetic of the two neutrino solutions gives the correct value in nearly 70% of the cases according to simulation. If there is no real solution to this quadratic equation, we alter our assumption of the W invariant mass. Imaginary solutions arise when the transverse mass is greater than the invariant mass. While this can not happen physically, detector resolution effects can cause the transverse mass to be reconstructed greater than the nominal mass. In these cases we change the assumption that led to the imaginary solution. We assume the invariant mass to be equal to the reconstructed tranverse mass. This causes the discriminant to vanish and we are left with two identical real solutions. It is important to note that this method differs from setting the discriminant to 0 by hand, since the real part of the solution depends on our assumption for the invariant mass as well. This method results in no events being discarded at this stage. The procedure described above is identical to Ref. [10]. Figure 1 shows the WZ invariant mass distributions for signal, background and data events for the combined channels after the WZ candidate selection. Figure 2 shows the four channels separately.

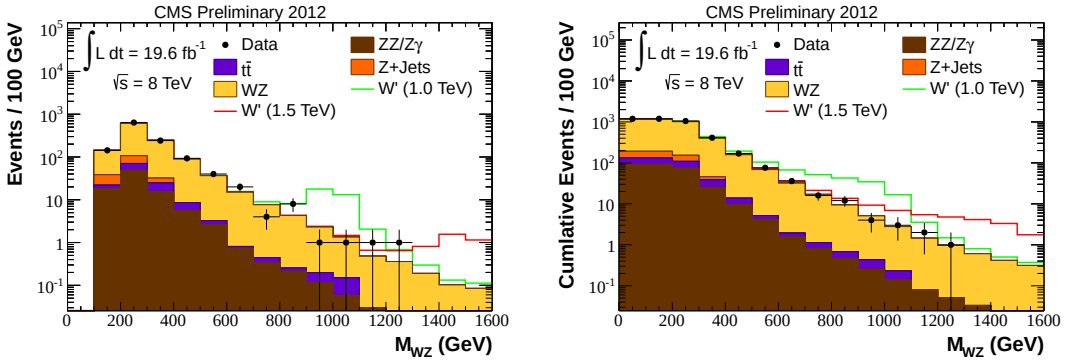

Figure 1: WZ invariant mass distributions for the MC background, signal and data after the WZ candidate selection for the combined channels (left) and the cumulative version (right). The last bin includes overflow events.

The event yields after applying the selection criteria listed above are given in Table 2. We break down this table by channel in Table 3.

In order to further suppress SM background events, we apply two additional selection requirements. The first is a requirement on L_{T}, the scalar sum of the charged leptons' transverse momenta (see Figs. 3, 4). The second is a requirement on the mass of the WZ system. The thresholds for these selection criteria were optimized at 100 GeV mass spacings for the WZ invariant mass ranging from 200 to 2000 GeV. Optimization entailed varying them both simultaneously in 50 GeV steps and optimizing for the best expected limit. The optimal values were then plotted as a function of the WZ mass in order to attempt to fit an analytic function to them. For the mass window requirement, two regimes of linear behavior were observed , corresponding to masses less than or greater than 1200 GeV: $0.2 \times M_{\mathrm{WZ}} - 20$ GeV and $1.45 \times M_{\mathrm{WZ}} - 1500$ GeV, respectively. For masses less than 1200 GeV, it is more optimal in terms of the expected limit to have a narrow mass window in order to reject as much background as possible. Above 1200 GeV, the background ceases to contribute significantly and it is much more optimal to have a large mass window. The L_{T} requirement shows a linear turn-on curve: $0.5 \times M_{\mathrm{WZ}} + 25\,\mathrm{GeV}$ for $M_{\mathrm{WZ}} < 1000\,\mathrm{GeV}$. As the mass increases, it becomes more optimal to require a larger L_{T}, until around 1000 GeV, at which point having L_{T} greater than 500 GeV is sufficient for producing an optimal limit. These mass window and L_{T} requirements are summarized in Table 4. The mass windows are displayed, along with the signal,

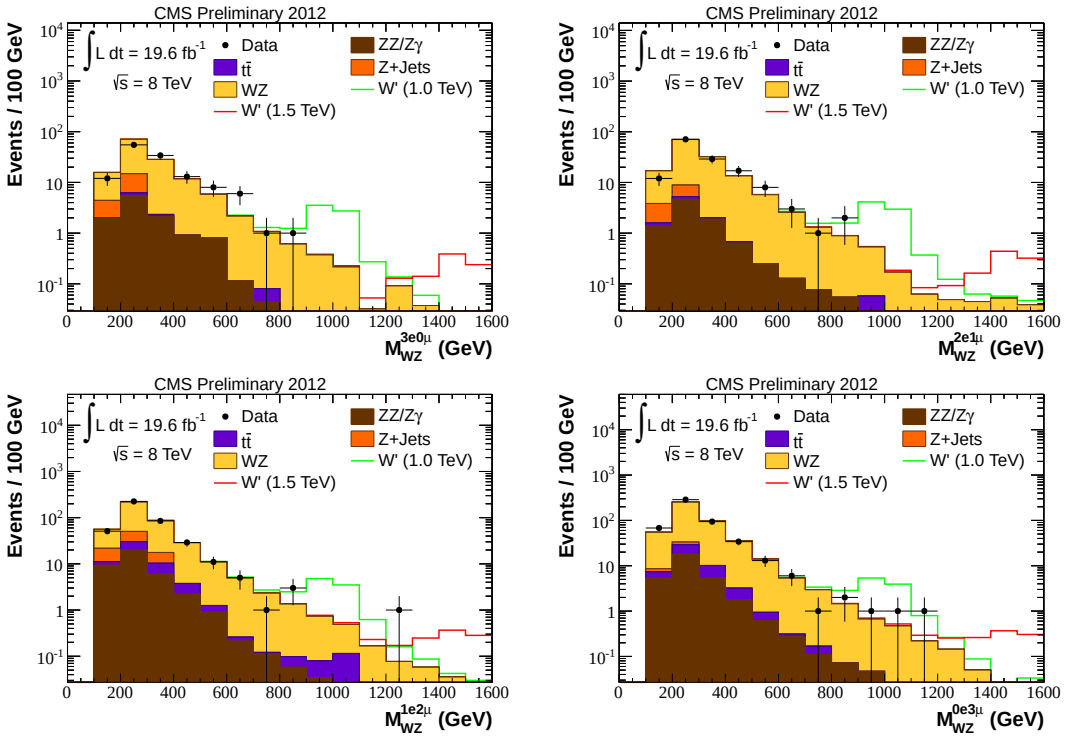

Figure 2: WZ invariant mass distributions for the MC background, signal and data after the WZ candidate selection for the $3e0\mu$ (top left), $2e1\mu$ (top right), $1e2\mu$ (bottom left) and $0e3\mu$ (bottom right) channels. The last bin includes overflow events.

Table 2: Observed events denoted as "Data", and expected signal and background yields after the main steps of the event selection with all channels combined. The numbers correspond to an integrated luminosity of 19.6 fb^{-1}. Errors indicated are statistical only.

Sample	Z Selection	W Selection	$E_{\mathrm{T}}^{\mathrm{miss}}$
Z + jets	2479 ± 80	254 ± 26	61 ± 13
$t\bar{t}$	141 ± 3	46 ± 1	39 ± 1
ZZ	504 ± 1	228.1 ± 0.7	72.5 ± 0.4
$Z\gamma$	302 ± 13	89 ± 7	19 ± 3
WZ	1694 ± 5	1298 ± 4	964 ± 3
Total Background	5120 ± 82	1915 ± 27	1156 ± 13
Data	5527	1992	1192
W′200	5014 ± 64	3840 ± 56	2516 ± 45
W′300	3211 ± 35	2868 ± 34	2360 ± 30
W′400	1397 ± 14	1288 ± 13	1155 ± 12
W′500	654 ± 6	615 ± 6	575 ± 5
W′600	327 ± 3	310 ± 3	295 ± 3
W′700	179 ± 1	171 ± 1	165 ± 1
W′800	102.7 ± 0.8	98.5 ± 0.8	95.5 ± 0.8
W′900	62.0 ± 0.5	59.6 ± 0.5	58.0 ± 0.5
W′1000	38.6 ± 0.3	37.2 ± 0.3	36.3 ± 0.3
W′1100	24.7 ± 0.2	23.9 ± 0.2	23.4 ± 0.2
W′1200	16.1 ± 0.1	15.5 ± 0.1	15.1 ± 0.1
W′1300	10.76 ± 0.08	10.37 ± 0.08	10.16 ± 0.08
W′1400	7.18 ± 0.06	6.88 ± 0.05	6.73 ± 0.05
W′1500	4.84 ± 0.04	4.61 ± 0.04	4.50 ± 0.04
W′1600	3.27 ± 0.03	3.11 ± 0.02	3.04 ± 0.02
W′1700	2.30 ± 0.02	2.18 ± 0.02	2.14 ± 0.02
W′1800	1.63 ± 0.01	1.54 ± 0.01	1.51 ± 0.01
W′1900	1.117 ± 0.009	1.053 ± 0.008	1.028 ± 0.008
W′2000	0.792 ± 0.006	0.746 ± 0.006	0.729 ± 0.006

Table 3: Observed events denoted as "Data", and expected signal and background yields after the $E_{\mathrm{T}}^{\mathrm{miss}}$ selection, broken down by channel. The numbers correspond to an integrated luminosity of 19.6 fb^{-1}. Errors indicated are statistical only.

Sample	$E_{\mathrm{T}}^{\mathrm{miss}}$			
	3e	2e1μ	1e2μ	3μ
Z + jets	11 ± 6	6 ± 4	38 ± 9	6 ± 4
$t\bar{t}$	0.9 ± 0.2	1.0 ± 0.2	18.1 ± 0.9	19.3 ± 0.9
ZZ	8.5 ± 0.1	9.1 ± 0.2	23.7 ± 0.3	31.2 ± 0.3
Zγ	3 ± 1	$\ll 0.1$	16 ± 3	0.5 ± 0.5
WZ	113 ± 1	128 ± 1	315 ± 2	408 ± 2
Total Background	137 ± 6	144 ± 4	410 ± 10	465 ± 5
Data	130	143	411	508
W$'$200	311 ± 16	300 ± 16	876 ± 27	1029 ± 29
W$'$300	310 ± 11	389 ± 12	735 ± 17	926 ± 19
W$'$400	185 ± 5	220 ± 5	336 ± 7	415 ± 7
W$'$500	103 ± 2	119 ± 3	158 ± 3	195 ± 3
W$'$600	53 ± 1	64 ± 1	81 ± 1	97 ± 2
W$'$700	31.7 ± 0.6	35.1 ± 0.7	44.5 ± 0.7	53.6 ± 0.8
W$'$800	18.4 ± 0.4	20.5 ± 0.4	25.7 ± 0.4	30.9 ± 0.5
W$'$900	11.2 ± 0.2	13.1 ± 0.2	15.8 ± 0.2	17.9 ± 0.3
W$'$1000	7.1 ± 0.1	8.1 ± 0.1	9.7 ± 0.2	11.4 ± 0.2
W$'$1100	4.66 ± 0.08	5.17 ± 0.09	6.3 ± 0.1	7.2 ± 0.1
W$'$1200	2.99 ± 0.05	3.38 ± 0.06	4.00 ± 0.06	4.77 ± 0.07
W$'$1300	1.99 ± 0.04	2.25 ± 0.04	2.78 ± 0.04	3.14 ± 0.04
W$'$1400	1.33 ± 0.02	1.51 ± 0.03	1.79 ± 0.03	2.09 ± 0.03
W$'$1500	0.89 ± 0.02	0.98 ± 0.02	1.24 ± 0.02	1.38 ± 0.02
W$'$1600	0.61 ± 0.01	0.66 ± 0.01	0.82 ± 0.01	0.96 ± 0.01
W$'$1700	0.429 ± 0.008	0.465 ± 0.008	0.578 ± 0.009	0.663 ± 0.009
W$'$1800	0.304 ± 0.005	0.324 ± 0.006	0.412 ± 0.006	0.470 ± 0.007
W$'$1900	0.204 ± 0.004	0.220 ± 0.004	0.274 ± 0.004	0.331 ± 0.005
W$'$2000	0.147 ± 0.003	0.154 ± 0.003	0.199 ± 0.003	0.230 ± 0.003

background and data distributions in Fig 5.

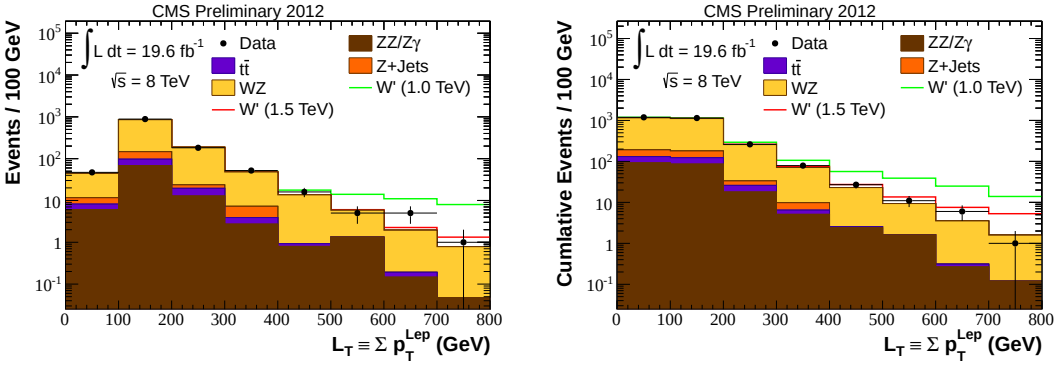

Figure 3: L_{T} for the MC background, signal and data after the WZ candidate selection criteria have been applied (left) and the cumulative distribution (right). The last bin includes overflow events.

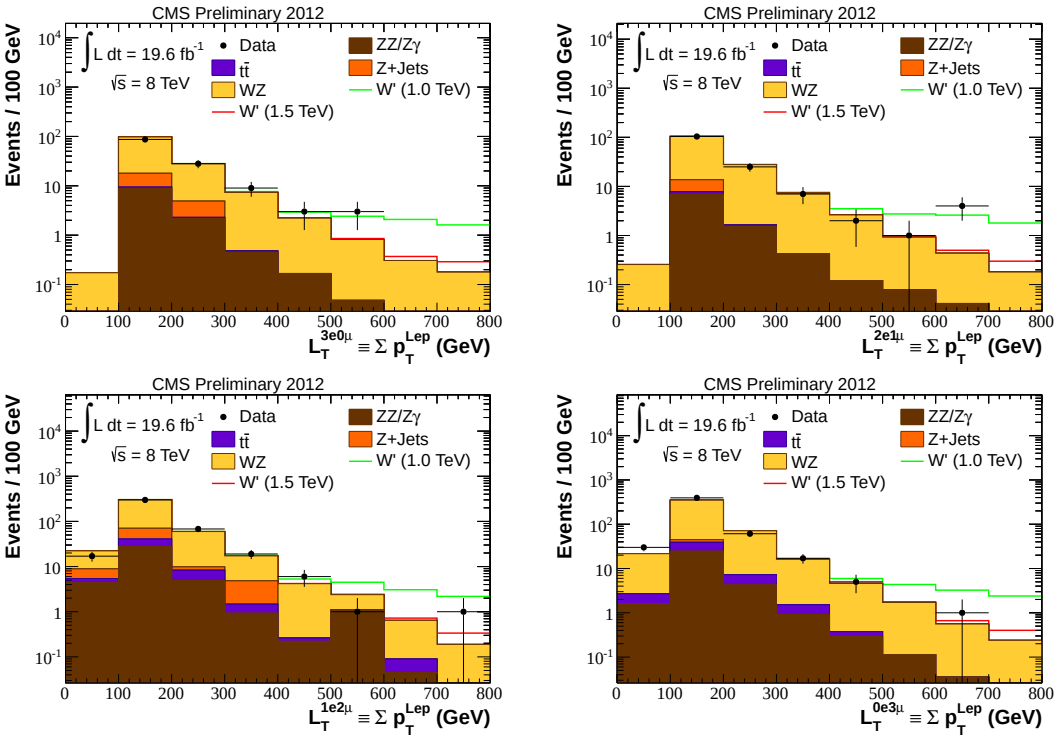

Figure 4: L_{T} for the MC background, signal and data after the WZ candidate selection criteria have been applied for the $3e0\mu$ (top left), $2e1\mu$ (top right), $1e2\mu$ (bottom left) and $0e3\mu$ (bottom right) channels. The last bin includes overflow events.

5 Systematic Uncertainties

Systematic uncertainties can be grouped into the following categories.

In the first group, we combine the uncertainties that affect the product of the acceptance, reconstruction, and identification efficiencies of final-state objects, as determined from simulation. These include uncertainties on lepton and $E_{\mathrm{T}}^{\mathrm{miss}}$ energy scales and resolution, as well as

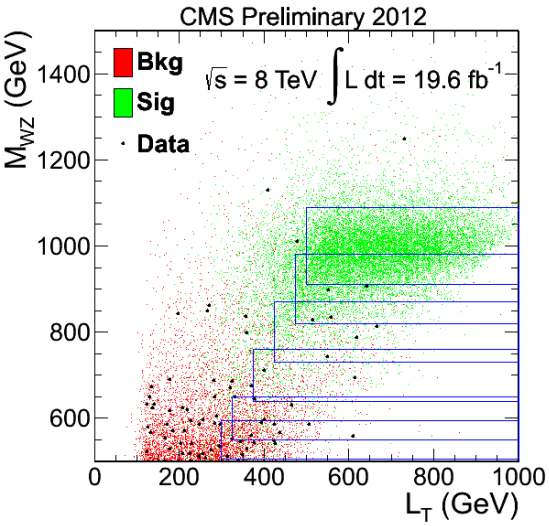

Figure 5: M_{WZ} versus L_{T} for the MC background, signal and data after the WZ candidate selection criteria have been applied.

theoretical uncertainties in the PDFs. We estimate the impact of the $E_{\mathrm{T}}^{\mathrm{miss}}$ scale and resolution uncertainties by varying the relevant parameter and measuring the effects on the yield of signal and background in MC for each mass point under consideration. Following the recommendations of the PDF4LHC group [28], PDF and α_s variations of the MSTW2008 [29], CT10 [30] and NNPDF2.0 [31] PDF sets were taken into account and their impact on the WZ cross section estimated. Signal PDF uncertainties are not taken into account with respect to the central limit, but are used to provide an uncertainty band around the signal cross section. An uncertainty associated with the simulation of pileup is also taken into account.

The second group includes the systematic uncertainties affecting the data vs. simulation correction factors for the efficiencies of the trigger, reconstruction, and identification requirements. These include lepton trigger, reconstruction and identification efficiencies. These efficiencies are derived from tag-and-probe studies and the uncertainty on the ratio of the efficiencies is typically taken as the systematic uncertainty. For the $\mathrm{Z} \to ee$ channel we apply a 2% uncertainty related to the trigger scale factors and another 2% to account for the difference in reconstruction efficiency between data and simulation. We apply an additional 1% uncertainty related to the electron identification and isolation scale factors. For the $\mathrm{Z} \to \mu\mu$ channel we apply a 5% uncertainty related to the trigger and another 2% uncertainty due to the differences in the efficiency of muon reconstruction for data and simulation. We also apply a conservative 3% uncertainty related to the scale factors for muon identification and isolation. This uncertainty is expected to cover potential differences related to the boosted topology of the signal.

The third category comprises uncertainties on the background yield. These are dominated by the theoretical uncertainties on the WZ component. We consider contributions coming from uncertainties on the choice of PDF (described above), renormalization and factorization scales, and on the WZ modeling in MADGRAPH. Scale uncertainties were determined by studying the variation of the cross section in the same analysis phase space by varying the renormalization and factorization scales by a factor of two upwards and downwards with respect to their nominal values. The largest observed variation is taken as a systematic uncertainty. This results in uncertainties of 5% for WZ masses up to 500 GeV and up to 15% from 600 GeV to 2 TeV. As the MADGRAPH sample used for simulating the WZ process contains explicit production of additional jets at matrix-element level, it provides an accurate description of the process which

includes higher-order corrections. The prediction is thus only rescaled with a global factor to the total NLO cross section computed with MCFM 6.6 [32]. To estimate uncertainties related to remaining modeling differences between the spectra predicted by MADGRAPH and true NLO predictions, we studied the ratio of the WZ cross section in the phase space defined by the analysis selection criteria (for each mass point) to the inclusive WZ cross section. We compared this ratio between MADGRAPH and MCFM. We found differences of order 5% for WZ masses up to 1 TeV, and of order 30% between 1 and 2 TeV. These differences are taken as additional systematic uncertainties on the SM WZ background. For the other background processes, the cross sections are varied by amounts estimated for the phase space relevant for this analysis as follows: ZZ and Z+jets by 30%, $\mathrm{t\bar{t}}$ by 15% and $Z\gamma$ by 50%.

Finally, an additional uncertainty of 4.4% is included due to the measurement of the integrated luminosity [33].

6 Results

We observe no significant excess in the data and calculate exclusion limits on the production cross section $\sigma(pp \to \mathrm{W}'/\rho_{\mathrm{TC}} \to \mathrm{WZ}) \times BR(\mathrm{WZ} \to 3\ell\nu)$ by using a cut-and-count method and comparing the numbers of observed events with the numbers of expected signal and background events. We use the background estimates as derived from the simulation.

Exclusion limits are calculated at the 95% confidence level (C.L.) by employing the `RooStats` [34] implementation of Bayesian statistics and a flat prior for the signal production cross section. The results for the combination of the four individual channels is given in Table 4. These results can then be interpreted in the context of various models.

The expected and observed exclusion limits for the combination of the four channels are shown in Fig. 6. The largest fluctuation comes from a small excess of signal-like events in the 730-980 GeV mass region (see Table 4). We exclude W′ bosons with masses between 170 and 1450 GeV in the SSM. For LSTC, with the chosen parameters $M(\pi_{\mathrm{TC}}) = \frac{3}{4}M(\rho_{\mathrm{TC}}) - 25\,\mathrm{GeV}$, ρ_{TC} hadrons with masses between 170 and 1125 GeV are excluded. Assuming leading order cross sections (i.e. without the k-factors listed in Table 1) we exclude W′ bosons with masses between 170 and 1400 GeV and ρ_{TC} hadrons with masses between 170 and 1100 GeV. Figure 7 also shows LSTC limits determined as a function of the ρ_{TC} and π_{TC} masses.

The W′ production cross section, as well as the branching fraction of $\mathrm{W}' \to \mathrm{WZ}$, are affected by the strength of the coupling between W′ and WZ that we refer to as W′WZ. If the value of the coupling is stronger than that predicted by the SSM, the observed and expected limits are more stringent. This is illustrated in Fig. 8, where a 95% C.L. lower limit on the W′WZ coupling is given as a function of the mass of the W′ resonance.

7 Conclusion

We have performed a search for new exotic particles decaying to the WZ final state with electrons and muons using 19.6 fb^{-1} of data collected by the CMS experiment at $\sqrt{s} = 8$ TeV. We find no significant excess in the mass distribution of the WZ candidates compared to the background expectation from standard model processes. We interpret the results in the context of different theoretical models and set lower bounds at the 95% C.L. on the masses of hypothetical particles decaying to the WZ tri-leptonic final state. Assuming the sequential standard model,

Table 4: Search windows for each W′ mass point giving the number of expected background events from MC, number of events observed, number of expected signal events from MC, signal efficiency, and the expected and observed exclusion limits on $\sigma \times BR(W' \rightarrow 3\ell\nu)$ at 95% C.L. for the combined channels. Errors indicated are statistical only.

Mass (GeV)	L_T (GeV)	Window (GeV)	N_{Bkg}	N_{Data}	N_{Sig}	ε_{Sig} (%)	$\sigma^{Exp.}_{Limit}$ (pb)	$\sigma^{Obs.}_{Limit}$ (pb)
W′170	110	163-177	9.1 ± 0.3	8	18 ± 1	1.33 ± 0.09	0.035	0.033
W′180	115	172-188	38 ± 2	49	141 ± 7	1.97 ± 0.09	0.056	0.082
W′190	120	181-199	62 ± 1	76	373 ± 14	2.6 ± 0.1	0.055	0.079
W′200	125	190-210	81 ± 4	86	613 ± 20	3.2 ± 0.1	0.054	0.065
W′210	130	199-221	86 ± 3	101	790 ± 24	3.9 ± 0.1	0.047	0.057
W′220	135	208-232	92 ± 4	84	901 ± 24	4.5 ± 0.1	0.043	0.035
W′230	140	217-243	93 ± 4	80	982 ± 25	5.2 ± 0.1	0.036	0.032
W′240	145	226-254	91 ± 4	84	1016 ± 24	5.8 ± 0.1	0.032	0.026
W′250	150	235-265	82 ± 1	85	1026 ± 23	6.4 ± 0.1	0.025	0.026
W′275	162	258-292	74 ± 3	85	975 ± 20	8.0 ± 0.2	0.019	0.024
W′300	175	280-320	60.8 ± 0.9	74	863 ± 16	9.6 ± 0.2	0.014	0.021
W′325	188	302-348	56 ± 3	53	797 ± 13	11.8 ± 0.2	0.011	0.0085
W′350	200	325-375	49 ± 3	37	703 ± 11	13.9 ± 0.2	0.0082	0.0044
W′400	225	370-430	32 ± 1	40	545 ± 7	18.1 ± 0.2	0.0047	0.0068
W′450	250	415-485	23.2 ± 0.8	26	401 ± 5	21.5 ± 0.2	0.0033	0.0042
W′500	275	460-540	16.7 ± 0.5	13	299 ± 3	24.8 ± 0.3	0.0024	0.0018
W′550	300	505-595	13.3 ± 0.6	14	221 ± 2	27.6 ± 0.3	0.0019	0.0021
W′600	325	550-650	10.1 ± 0.5	10	168 ± 2	30.4 ± 0.3	0.0016	0.0016
W′700	375	640-760	4.8 ± 0.2	4	97.4 ± 0.8	34.3 ± 0.3	0.00099	0.00091
W′800	425	730-870	2.8 ± 0.2	5	56.8 ± 0.5	36.5 ± 0.3	0.00078	0.0012
W′900	475	820-980	2.1 ± 0.2	4	35.2 ± 0.3	38.6 ± 0.3	0.00066	0.00099
W′1000	500	910-1090	1.4 ± 0.1	0	23.8 ± 0.2	43.3 ± 0.3	0.00050	0.00036
W′1100	500	1000-1200	0.8 ± 0.1	0	15.9 ± 0.1	46.8 ± 0.3	0.00045	0.00033
W′1200	500	1080-1320	0.58 ± 0.08	1	10.83 ± 0.07	49.1 ± 0.3	0.00033	0.00045
W′1300	500	1108-1492	0.56 ± 0.08	1	8.25 ± 0.04	56.1 ± 0.3	0.00029	0.00039
W′1400	500	1135-1665	0.60 ± 0.08	1	5.67 ± 0.03	57.3 ± 0.3	0.00028	0.00039
W′1500	500	1162-1838	0.57 ± 0.08	1	3.78 ± 0.02	57.5 ± 0.3	0.00028	0.00038
W′1600	500	1190-2010	0.56 ± 0.08	1	2.58 ± 0.01	57.7 ± 0.3	0.00028	0.00039
W′1700	500	1218-2182	0.51 ± 0.08	1	1.791 ± 0.009	57.6 ± 0.3	0.00028	0.00039
W′1800	500	1245-2355	0.44 ± 0.07	1	1.262 ± 0.007	58.0 ± 0.3	0.00027	0.00039
W′1900	500	1272-2528	0.39 ± 0.07	0	0.848 ± 0.005	55.0 ± 0.3	0.00029	0.00029
W′2000	500	1300-2700	0.36 ± 0.07	0	0.598 ± 0.003	54.7 ± 0.3	0.00029	0.00029

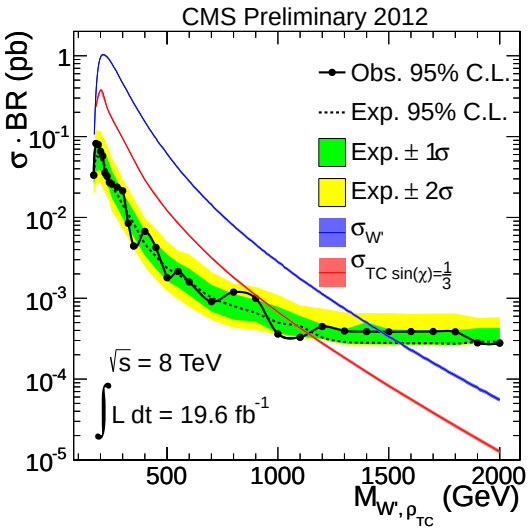

Figure 6: Expected and observed exclusion limit on $\sigma \times BR(\mathrm{W}' \to 3\ell\nu)$ as a function of the WZ mass for W' and ρ_{TC}, along with the combined $1\,\sigma$ ($2\,\sigma$) statistical and systematic uncertainties depicted with the green (yellow) band.

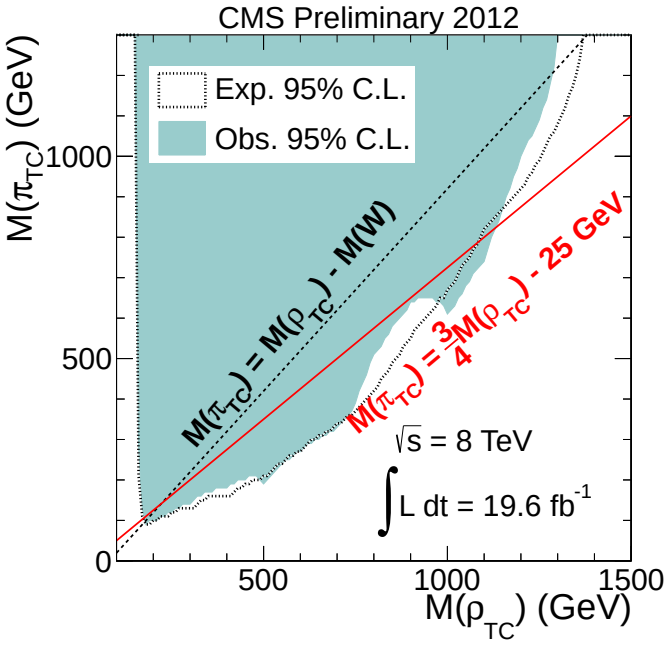

Figure 7: Two-dimensional exclusion limit for LSTC as a function of the ρ_{TC} and π_{TC} masses.

we exclude W' bosons with masses between 170 and 1450 GeV. We also exclude technicolor ρ_{TC} hadrons with masses between 170 and 1125 GeV assuming $M(\pi_{\mathrm{TC}}) = \frac{3}{4}M(\rho_{\mathrm{TC}}) - 25\,\mathrm{GeV}$. These are the most restrictive limits to date in the WZ channel.

References

[1] J. C. Pati and A. Salam, "Lepton number as the fourth 'color' ", *Phys. Rev. D* **10** (1974) 275, doi:10.1103/PhysRevD.10.275. Erratum-ibid. D **11** (1975) 703.

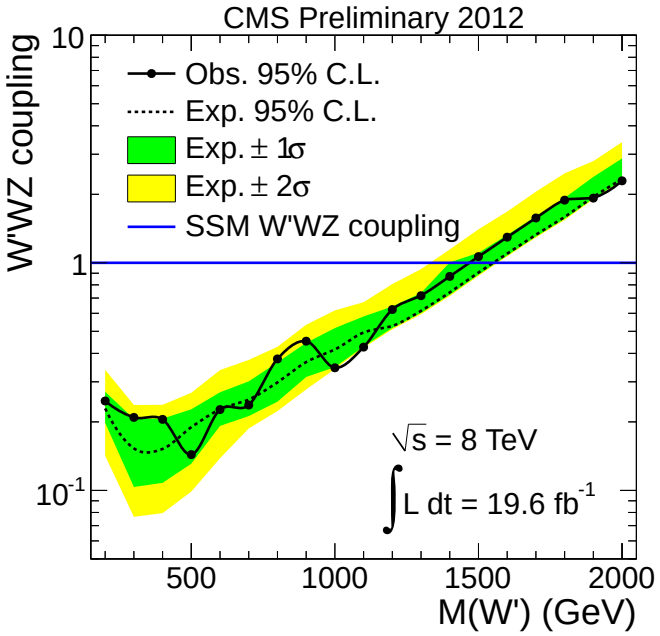

Figure 8: 95% C.L. lower limit on the strength of W′WZ coupling normalized to the SSM prediction as a function of the W′ mass.

[2] G. Altarelli, B. Mele, and M. Ruiz-Altaba, "Searching for new heavy vector bosons in $p\bar{p}$ colliders", *Z. Phys. C* **45** (1989) 109, doi:10.1007/BF01556677. Erratum-ibid. C **47** (1990) 676.

[3] A. Birkedal, K. Matchev, and M. Perelstein, "Collider phenomenology of the Higgsless models", *Phys. Rev. Lett.* **94** (2005) 191803, doi:10.1103/PhysRevLett.94.191803, arXiv:hep-ph/0412278.

[4] M. Perelstein, "Little Higgs models and their phenomenology", *Prog. Part. Nucl. Phys.* **58** (2007) 247, doi:10.1016/j.ppnp.2006.04.001, arXiv:hep-ph/0512128.

[5] K. Agashe et al., "LHC Signals for Warped Electroweak Charged Gauge Bosons", *Phys. Rev. D* **80** (2009) 075007, doi:10.1103/PhysRevD.80.075007, arXiv:0810.1497.

[6] C. Grojean, E. Salvioni, and R. Torre, "A weakly constrained W' at the early LHC", *JHEP* **07** (2011) 002, doi:10.1007/JHEP07(2011)002, arXiv:1103.2761v3.

[7] D0 Collaboration, "Search for a resonance decaying into WZ boson pairs in $p\bar{p}$ collisions", *Phys. Rev. Lett.* **104** (2010) 061801, doi:10.1103/PhysRevLett.104.061801, arXiv:0912.0715v3.

[8] CDF Collaboration, "Search for WW and WZ Resonances Decaying to Electron, Missing E_T, and Two Jets in $p\overline{p}$ Collisions at $\sqrt{s} = 1.96$ TeV.", *Phys. Rev. Lett.* **104** (2010) 241801, doi:10.1103/PhysRevLett.104.241801, arXiv:1004.4946.

[9] ATLAS Collaboration, "Search for resonant WZ production in the $WZ \to \ell\nu\ell'\ell'$ channel in $\sqrt{s} = 7$ TeV pp collisions with the ATLAS detector", *Phys. Rev. D* **85** (2012) 112012, doi:10.1103/PhysRevD.85.112012, arXiv:1204.1648.

[10] CMS Collaboration, "Search for a W' or Techni-ρ Decaying into WZ in pp Collisions at $\sqrt{s} = 7$ TeV", *Phys. Rev. Lett.* **109** (2012) 141801, doi:10.1103/PhysRevLett.109.141801, arXiv:1206.0433.

[11] CMS Collaboration, "Search for exotic resonances decaying into WZ/ZZ in pp collisions at $\sqrt{s} = 7$ TeV", *JHEP* **1302** (2013) 036, doi:10.1007/JHEP02(2013)036, arXiv:1211.5779.

[12] K. Lane, "Technihadron production and decay in low-scale technicolor", *Phys. Rev. D* **60** (1999) 075007, doi:10.1103/PhysRevD.60.075007.

[13] E. Eichten and K. Lane, "Low-scale technicolor at the Tevatron and LHC", *Phys. Lett. B* **669** (2008) 235, doi:10.1016/j.physletb.2008.09.047, arXiv:0706.2339.

[14] CMS Collaboration, "The CMS experiment at the CERN LHC", *JINST* **3** (2008) S08004, doi:10.1088/1748-0221/3/08/S08004.

[15] S. J. Allison et al., "Geant4 Developments and Applications", *IEEE Trans. Nucl. Sci.* **53** (2006) 270.

[16] S. M. T. Sjőstrand and P. Z. Skands, "PYTHIA 6.4 Physics and Manual", *JHEP* **0605** (2006) doi:10.1088/1126-6708/2006/05/026.

[17] J. Pumplin et al., "New generation of parton distributions with uncertainties from global QCD analysis", *JHEP* **0207** (2002) 012, arXiv:hep-ph/0201195.

[18] CMS Collaboration, "Measurement of the underlying event activity at the LHC with $\sqrt{s}$=7 TeV and comparison with $\sqrt{s}$=0.9 TeV", *JHEP* **09** (2011) 109, doi:10.1007/JHEP09(2011)109, arXiv:1107.0330.

[19] R. Gavin et al., "FEWZ 2.0: A code for hadronic Z production at next-to- next-to-leading order", *Comput. Phys. Commun.* **182** (2011) 2388–2403, doi:10.1016/j.cpc.2011.06.008.

[20] New Physics Working Group Collaboration, "New Physics at the LHC. A Les Houches Report: Physics at TeV Colliders 2009 - New Physics Working Group", (2010). arXiv:1005.1229.

[21] J. Alwall et al., "MadGraph/MadEvent v4: The New Web Generation", *JHEP* **09** (2007) 028, doi:10.1088/1126-6708/2007/09/028.

[22] S. Frixione, P. Nason, and C. Oleari, "Matching NLO QCD computations with Parton Shower simulations: the POWHEG method", *JHEP* **11** (2007) 070, doi:10.1088/1126-6708/2007/11/070.

[23] CMS Collaboration, "Commissioning of the particle-flow event reconstruction with leptons from J/ψ and W decays at 7 TeV", (2010). CMS-PAS-PFT-10-003.

[24] CMS Collaboration, "Particle-Flow Event Reconstruction in CMS and Performance for Jets, Taus, and Missing ET", (2009). CMS-PAS-PFT-09-001.

[25] CMS Collaboration, "Performance of CMS muon reconstruction in pp collision events at $\sqrt{s} = 7$ TeV", *JINST* **7** (2012) P10002, doi:10.1088/1748-0221/7/10/P10002, arXiv:1206.4071.

[26] CMS Collaboration, "Measurement of the Inclusive W and Z Production Cross Sections in pp Collisions at $\sqrt{s} = 7$ TeV", *JHEP* **1110** (2011) 132, doi:10.1007/JHEP10(2011)132, arXiv:1107.4789.

[27] W. Adam et al., "Reconstruction of electrons with the Gaussian sum filter in the CMS tracker at LHC", *J. Phys G* **31** (2005) doi:10.1088/0954-3899/31/9/N01,10.1088/0954-3899/31/9/N01, arXiv:physics/0306087.

[28] M. Botje et al., "The PDF4LHC Working Group Interim Recommendations", (2011). arXiv:1101.0538v1.

[29] A. D. Martin et al., "Parton distributions for the LHC", *Eur. Phys. J. C* **63** (2009) 189, doi:10.1140/epjc/s10052-009-1072-5, arXiv:0901.0002.

[30] P. M. Nadolsky et al., "Implications of CTEQ global analysis for collider observables", *Phys. Rev. D* **78** (2008) 013004, doi:10.1103/PhysRevD.78.013004, arXiv:0802.0007.

[31] R. D. Ball et al., "A first unbiased global NLO determination of parton distributions and their uncertainties", *Nucl. Phys. B* **838** (2010) 136, doi:10.1016/j.nuclphysb.2010.05.008, arXiv:1002.4407.

[32] J. M. Campbell and R. K. Ellis, "MCFM for the Tevatron and the LHC", *Nucl. Phys. Proc. Suppl.* **205-206** (2010) 10–15, doi:10.1016/j.nuclphysbps.2010.08.011, arXiv:1007.3492.

[33] CMS Collaboration, "CMS Luminosity Based on Pixel Cluster Counting - Summer 2012 Update", (2012). CMS-PAS-LUM-12-001.

[34] L. Moneta et al. , "The RooStats Project", *ACAT2010 Conference Proceedings* (2011) arXiv:arXiv:1009.1003v1.